# X-ray determination of threading dislocation densities in GaN/Al2O3(0001) films grown by metalorganic vapor phase epitaxy

Viktor S. Kopp, Vladimir M. Kaganer, Marina V. Baidakova, Wsevolod V. Lundin, Andrey E. Nikolaev, Elena V. Verkhovtceva, Maria A. Yagovkina, Nikolay Cherkashin

# X-ray determination of threading dislocation densities in GaN/$Al_2O_3$(0001) films grown by metalorganic vapor phase epitaxy

Viktor S. Kopp, Vladimir M. Kaganer, Marina V. Baidakova, Wsevolod V. Lundin, Andrey E. Nikolaev, Elena V. Verkhovtceva, Maria A. Yagovkina, and Nikolay Cherkashin

Citation: Journal of Applied Physics **115**, 073507 (2014); doi: 10.1063/1.4865502
View online: https://doi.org/10.1063/1.4865502
View Table of Contents: http://aip.scitation.org/toc/jap/115/7
Published by the American Institute of Physics

# X-ray determination of threading dislocation densities in GaN/$Al_2O_3$(0001) films grown by metalorganic vapor phase epitaxy

Viktor S. Kopp,[1,a)] Vladimir M. Kaganer,[1] Marina V. Baidakova,[2] Wsevolod V. Lundin,[2] Andrey E. Nikolaev,[2] Elena V. Verkhovtceva,[2] Maria A. Yagovkina,[2] and Nikolay Cherkashin[3]

[1]*Paul-Drude-Institut für Festkörperelektronik, Hausvogteiplatz 5–7, 10117 Berlin, Germany*
[2]*Ioffe Physical-Technical Institute of the Russian Academy of Sciences, Politekhnicheskaya 26, 194021 St.-Petersburg, Russia*
[3]*CEMES-CNRS and Université de Toulouse, 29 rue J. Marvig, 31055 Toulouse, France*

(Received 9 December 2013; accepted 31 January 2014; published online 19 February 2014)

Densities of a- and a+c-type threading dislocations for a series of GaN films grown in different modes by metalorganic vapor phase epitaxy are determined from the x-ray diffraction profiles in skew geometry. The reciprocal space maps are also studied. Theory of x-ray scattering from crystals with dislocations is extended in order to take into account contribution from both threading and misfit dislocations. The broadening of the reciprocal space maps along the surface normal and the rotation of the intensity distribution ellipse is attributed to misfit dislocations at the interface. We find that the presence of a sharp AlN/GaN interface leads to an ordering of misfit dislocations and reduces strain inhomogeneity in GaN films. © *2014 AIP Publishing LLC*.
[http://dx.doi.org/10.1063/1.4865502]

## I. INTRODUCTION

The increasing range of applications of GaN–based structures such as light emitting diodes, lasers and high power transistors requires the study of the influence of extended defects on the electrical and optical properties of these materials.[1,2] The most important extended defects in these structures are threading dislocations. Their total density in GaN(0001) epitaxial layers varies typically in the range from $10^8$ to $10^{10}$ $cm^{-2}$, with the density of edge threading dislocations exceeding the density of screw and mixed dislocations. It is well documented that threading dislocations in GaN act as nonradiative recombination centers, determine the minority carrier diffusion length and limit the device performance (see Ref. 3 and references therein). Thus, the reliable determination of threading dislocation densities could help to understand their effect on the device performance of GaN films.

X-ray diffraction is commonly used to investigate the structural quality of GaN films (see, e.g., Ref. 4 for a review). Special efforts are made to reveal threading dislocations. Edge threading dislocations, with the lines perpendicular to the film surface, are not visible in symmetric Bragg reflections. A special diffraction geometry, called skew geometry, was proposed to uncover these dislocations.[5] The measurement of the diffraction peak width allows one to compare structural quality of different films, but an interpretation of the peak width in terms of dislocation density is not straightforward. In many studies, the interpretation is based on the mosaic block model.[6–9] Determination of the dislocation densities from peak widths[9–12] is based on different variants of the formulas proposed for the classical models in powder diffraction.[13–15]

A direct Monte Carlo calculation of the diffraction peak profile due to parallel straight dislocations demonstrates that the peak width depends not only on the dislocation density but also on the spatial correlations in dislocation positions.[16] The dislocation density can be determined, together with an estimate of the dislocation correlations, from the whole diffraction profile including its asymptotes, rather than just from the peak width.[17] The double-crystal peak profiles measured in skew geometry are most suitable for this purpose. The dislocation density determination has been tested on GaN films with densities of threading dislocations exceeding $10^{10}$ $cm^{-2}$ and with density of edge dislocations an order of magnitude larger than the density of screw dislocations.[17,18]

The aim of the present paper is to develop a method for the determination of dislocation density from x-ray diffraction data for the technologically relevant GaN films grown by metalorganic vapor phase epitaxy (MOVPE). The densities of threading dislocations in these films are 1–2 orders of magnitude smaller than in previously analysed samples,[17] and the densities of edge and screw dislocations can be comparable. We find that the lower dislocation densities do not restrict the applicability of the method. Particularly, we demonstrate by Monte Carlo calculations that the elastic strain relaxation at the free surface has a minor effect on the double-crystal diffraction profiles. On the other hand, it is not possible to study separately screw dislocations in symmetric reflections and edge dislocations in asymmetric reflections, as it was done in Refs. 17 and 18. Comparable densities of the screw and the edge components of the Burgers vectors require to take into account all dislocations in the calculation of asymmetric reflections simultaneously. Reciprocal space maps are also investigated. We show that they cannot be explained by only threading dislocations and require to take into account the effect of interfacial misfit dislocations.

[a)]Electronic mail: victor.kopp@pdi-berlin.de.

 

## II. EXPERIMENTAL

The epitaxial structures studied in the present paper were grown by MOVPE in an AIX2000HT system with a planetary reactor for six 2-in. substrates. Ammonia, trimethylgallium, and trimethylaluminum were used as precursors, hydrogen and nitrogen as carrier gases. Four different epitaxial structures were grown on (0001) sapphire substrates.

Epitaxy of the sample 1 begins with the growth of an atomically smooth 300 nm thick AlN film at a high growth rate of 2 $\mu$m/h.[19] The high-temperature growth of GaN on the AlN surface initially takes place in the 3D growth mode with a subsequent planarization. This technique is a good alternative to the standard one for LED fabrication, allowing us to avoid the thermocycling of reactor (temperature reduction for nucleation layer deposition and rise for its annealing) and possessing a shorter process time.

Growth of the sample 2 is similar, but the AlN layer was grown in a different regime resulting in its roughening.[19] The subsequent high-temperature GaN layer is grown in the quasi-2D-mode from the very beginning. Such GaN layers are highly resistive and may be used for high electron mobility transistors.

Sample 3 was grown using a standard low-temperature GaN nucleation layer. After its deposition, the sample was annealed under $H_2$+$NH_3$ ambient. Decomposition of GaN due to interaction with hydrogen results in the formation of a dense array of separate nuclei. The consequent high-temperature growth was initiated on these nuclei and thus was initially of 3D nature followed by the coalescence of crystallites, planarization and 2D GaN growth. This is a standard technique for III-N LED manufacturing.

Finally, the growth process for sample 4 was especially developed for the growth of thin (~100 nm) layers of GaN on the top of thick (0.3–1 $\mu$m) AlN layers. The thickness of AlN layer of sample 4 is 0.9 $\mu$m. To avoid the island growth mode of GaN described above and obtain a smooth AlN layer, a 30 nm thick $Al_{0.3}Ga_{0.7}N$ transition layer was grown. This layer forms a continuous film and promotes 2D growth of the subsequent GaN layer. In the present case, a 3 $\mu$m thick GaN layer was grown on the AlGaN buffer.

Transmission electron microscopy (TEM) investigations were carried out with a 200 keV JEOL 2010 TEM. Specimens were prepared by tripod polishing and argon ion-beam thinning (Gatan PIPS) to about 250 nm thickness for cross-sectional $(01\bar{1}0)$ weak-beam dark-field observations of dislocations with diffraction vectors $\mathbf{g} = 2\bar{1}\bar{1}0$ and $\mathbf{g} = 0002$. The specimen thicknesses were measured in dark field using the extinction fringes of the reflection $\mathbf{g} = 0002$ in exact Bragg conditions. Edge a-type dislocations with Burgers vectors $\frac{1}{3}\langle 11\bar{2}0\rangle$ are visible in the images taken with $\mathbf{g} = 2\bar{1}\bar{1}0$, while screw c-type dislocations with Burgers

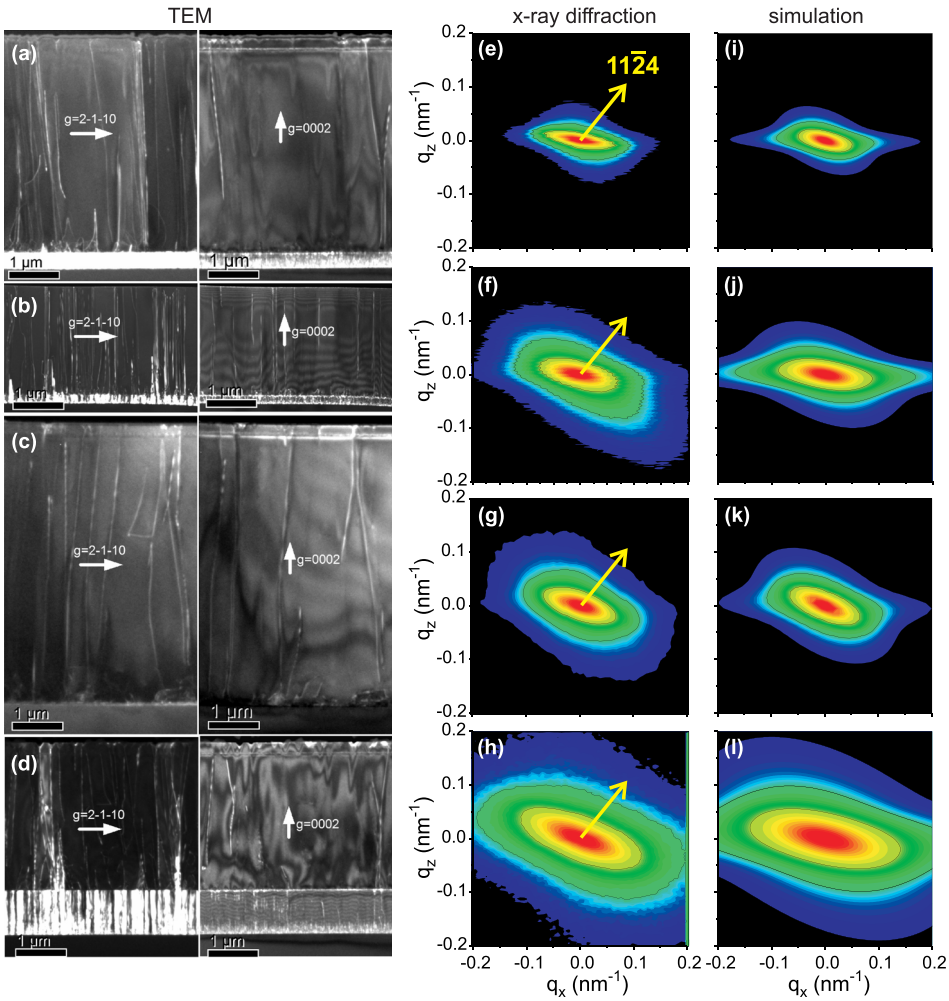


FIG. 1. Cross-sectional TEM images (left column), measured (middle column) and simulated (right column) reciprocal space maps of the 11$\bar{2}$4 reflection. Four rows present the data for samples 1–4.

vectors $\langle 0001\rangle$ are visible with $\mathbf{g} = 0002$ and mixed a+c-type dislocations with Burgers vectors $\frac{1}{3}\langle 11\bar{2}3\rangle$ are visible with both diffraction vectors. Using these dislocation visibility criteria, the densities of different type dislocations were determined. The error in the determination of the absolute values of the dislocation densities comes mainly from an uncertainty in the determination of a specimen thickness and is about 20%. However, the ratio of the densities of different type dislocations is determined with a higher precision since the measurements are carried out at the same area of a TEM specimen. The left column in Fig. 1 presents the set of cross-sectional $(01\bar{1}0)$ weak-beam dark-field images of samples 1–4. The images reveal that only edge a-type and mixed a+c-type dislocations are present in all samples. The absolute values of their densities are given in Table I. Dislocations presented in the highly defective regions close to the $Al_2O_3$/GaN interface were not taken into account for the dislocation density calculation.

X-ray measurements were performed using high resolution x-ray diffractometer (Bruker D8 Discover) equipped with an Eulerian quarter circle, a graded parabolic mirror and a double-crystal symmetric Ge (220) monochromator. Cu$K\alpha_1$ radiation from a 6 kW rotating anode x-ray source was used. Diffraction curves were recorded in symmetric skew geometry[5,20] either with a wide open detector (double–crystal diffractometry) at a fixed position $2\theta_B$ or with three-bounce Ge(220) analyzer crystal (triple–crystal diffractometry). Reciprocal space maps were recorded in coplanar diffraction geometry using the analyzer crystal. They are presented in the middle column of Fig. 1 and analyzed below in Sec. IV.

## III. DIFFRACTION PROFILES IN SKEW GEOMETRY

### A. Double-crystal diffraction

Figure 2 presents double–crystal x-ray diffraction peak profiles measured in the skew geometry.[5] Figure 2(a) compares different reflections from sample 1, while Figs. 2(b) and 2(c) compare $20\bar{2}1$ and $11\bar{2}4$ reflections for samples 1–4. For the analysis of the profiles we modify, after Ref. 17, the expressions for the x-ray intensity to take into account the contributions of both edge and screw components of the Burgers vectors for the asymmetric reflections. Instead of Eq. (10) in Ref. 17, we present the scattered intensity as a Fourier transformation

$$I(\omega) = \frac{I_i}{\pi}\int_0^\infty G_{\text{th}}(x)\cos(\omega x)\,dx + I_{\text{backgr}}, \tag{1}$$

of the correlation function for both a-type edge and a+c-type mixed threading dislocations,

$$G_{\text{th}}(x) = \exp\left(-A_e x^2 \ln\frac{B_e + x}{x} - A_{me} x^2 \ln\frac{B_{me} + x}{x} - A_{ms} x^2 \ln\frac{B_{ms} + x}{x}\right). \tag{2}$$

Here $\omega$ is the angular deviation of the sample from the Bragg position, $I(\omega)$ is the diffracted intensity, $I_i$ is the integrated intensity of the peak, and $I_{\text{backgr}}$ is the background intensity. In Eq. (1), we introduce, instead of one parameter $A$ for the dislocation density as in Ref. 17, three parameters $A_e, A_{me}, A_{ms}$ to describe edge dislocations, and the edge and screw components of mixed dislocations, respectively. Similarly, instead of one parameter $B$ for the dislocation correlation range, we introduce three parameters, $B_e, B_{me}, B_{ms}$. These parameters are expressed as

$$A_e = \gamma_e f \rho_e b_e^2,\ A_{me} = \gamma_e f \rho_m b_e^2,\ A_{ms} = \gamma_s f \rho_m b_s^2,$$
$$B_e = gR_e/b_e,\ B_{me} = gR_m/b_e,\ B_{ms} = gR_m \tan\Psi/b_s, \tag{3}$$

where $\rho_e$ and $\rho_m$ are the densities of edge and mixed threading dislocations, $R_e$ and $R_m$ are the characteristic distances for the screening of the dislocation strain fields, $b_e$ and $b_s$ are the lengths of the edge and the screw components of the Burgers vectors, and

$$f = \frac{\cos^2\Phi}{4\pi\cos^2\theta_B},\ g = \frac{2\pi\cos\theta_B}{\cos\Phi\cos\Psi}. \tag{4}$$

The notation of angles follows that of Ref. 17: $\Phi$ is the angle between the diffracted beam and the film surface, $\Psi$ is the angle between the diffraction vector and the film surface, $\theta_B$ is the Bragg angle.

Equation (3) contains the factors $\gamma_e$ for edge and $\gamma_s$ screw components of the Burgers vectors that depend on the relative orientation of the vectors involved in the problem: the respective Burgers vector $\mathbf{b}$, the diffraction vector $\mathbf{Q}$ and the direction of the diffracted wave $\mathbf{K}^{\text{out}}$. Calculation of these factors (also called the contrast factors) is a bulky problem in the analysis of diffraction from dislocation ensembles (see Ref. 21 and references in it). The factor $\gamma_e$ calculated in Ref. 17 contains an error in one of the

TABLE I. Densities of edge and mixed threading dislocations measured by TEM, dislocation densities and correlation parameters obtained by fits of rocking curves in double–crystal x-ray diffraction, and the effective misfit dislocation densities evaluated from the reciprocal space maps.

| | | a–type dislocations | | | a+c–type dislocations | | | Effective |
|---|---|---|---|---|---|---|---|---|
| | | TEM | XRD | | TEM | XRD | | misfit dislocation |
| Sample | Thickness ($\mu$m) | density ($\times 10^8$cm$^{-2}$) | density ($\times 10^8$cm$^{-2}$) | Correlation $M$ | density ($\times 10^8$cm$^{-2}$) | density ($\times 10^8$cm$^{-2}$) | correlation $M$ | density ($\times 10^5$cm$^{-1}$) |
| 1 | 4.3 | 23.0 | $17.0 \pm 2.8$ | $18.5 \pm 11.0$ | 1.0 | 1.8 | 4.5 | 0.3 |
| 2 | 2.5 | 40.0 | $11.6 \pm 1.9$ | $3.9 \pm 1.9$ | 10.0 | 13.0 | 10.0 | 0.5 |
| 3 | 5.7 | 4.3 | $6.7 \pm 1.5$ | $11.0 \pm 9.1$ | 3.5 | 8.0 | 5.3 | 1.5 |
| 4 | 3.0 | 28.3 | $45.7 \pm 1.3$ | $7.7 \pm 5.0$ | 3.7 | 21.0 | 18.0 | 2.3 |

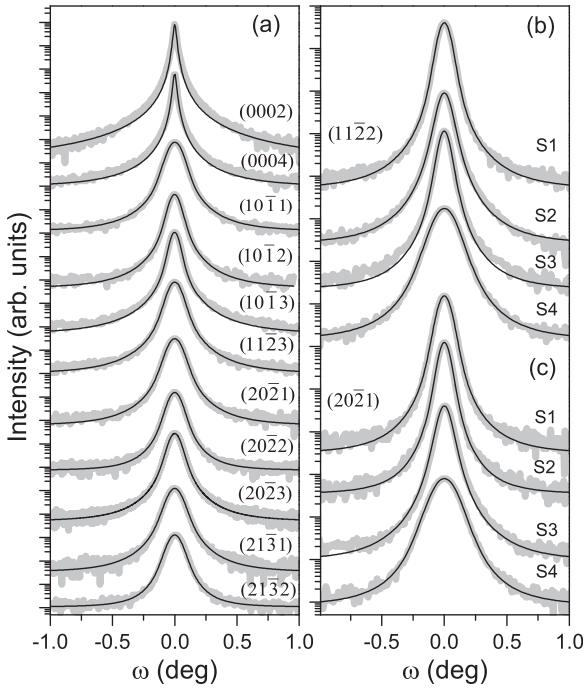


FIG. 2. Double-crystal rocking curves in skew geometry (a) for sample 1 and (b) and (c) for samples 1–4. The experimental profiles are shown by thick gray lines, red lines are fits.

coefficients. Here, we calculate the factors $\gamma_e$ and $\gamma_s$ in a slightly another way.

The factor $\gamma$ for a given dislocation array depends on the orientation of the Burgers vector **b**, the diffraction vector **Q**, and on the orientation of the two-dimensional vector $\rho$ in the plane perpendicular to dislocation lines. This vector defines the direction in which the displacement correlations are sought. The factor $\gamma$ is defined as

$$\gamma = \frac{1}{2\pi Qb\rho}\int_0^{2\pi} d\varphi \left(\rho_i \frac{\partial u_j}{\partial \rho_i} Q_j\right)^2, \tag{5}$$

where $\mathbf{u}(\rho)$ is the displacement field due to an individual dislocation. For edge dislocations in an isotropic medium, with the $z$ axis in the direction of dislocation lines and the $x$ axis along Burgers vector, this factor is calculated as[22]

$$\begin{aligned}\gamma = \frac{1}{16Q^2(1-\nu)^2}[&(9-16\nu+8\nu^2)Q_x^2 \\ &+(3-8\nu+8\nu^2)Q_y^2 - 2Q_xQ_y(3-4\nu)\sin 2\phi \\ &+2\left((1-2\nu)Q_y^2 - 2(1-\nu)Q_x^2\right)\cos 2\phi],\end{aligned} \tag{6}$$

where $\nu$ is the Poisson ratio and $\phi$ is the angle between vectors **b** and $\rho$.

The average of Eq. (6) over six orientations of the Burgers vectors $\frac{1}{3}\langle 11\bar{2}0\rangle$ in the coordinate system with the $x$ axis chosen along the projection of the diffracted beam direction $\mathbf{K}^{\text{out}}$ on the surface plane gives

$$\gamma_e = \frac{9-16\nu+8\nu^2-2(3-4\nu)\cos^2\alpha}{16(1-\nu)^2}\cos^2\Psi, \tag{7}$$

where $\alpha$ is the angle between projections of the scattering vector **Q** and the wave vector of the diffracted wave $\mathbf{K}^{\text{out}}$ on the surface plane. Equation (7) corrects the corresponding expression in Ref. 17 in the term $-16\nu$, instead of $-8\nu$.

For screw dislocations, one has[22] $\gamma = \frac{1}{2}(Q_z/Q)^2$ and thus

$$\gamma_s = \frac{1}{2}\sin^2\Psi. \tag{8}$$

The cross term between screw and edge Burgers vector components of mixed dislocations in Eq. (5) vanish after averaging over six orientations of the Burgers vector in the hexagonal crystal.

Figure 2 shows fits of Eq. (1) to the measured diffraction peak profiles. The fits are performed as follows. First, the symmetric Bragg reflections are fitted. Since edge dislocations and the edge components of the mixed dislocations do not contribute to symmetric reflections (because of $\mathbf{Q}\cdot\mathbf{u}=0$), only the screw components of the mixed dislocations are taken into consideration. In the peak profile analysis, it is not possible to distinguish between mixed a+c-dislocations with a density $\rho_m$ and separate a- and c-dislocations with the densities $\rho_m$ each. Since the TEM analysis reveals mixed and edge dislocations in the samples under consideration, we perform the x-ray analysis in terms of the same dislocation types, to facilitate a comparison of the results. The x-ray diffraction profiles can be equally well described by c-type screw dislocations with the density $\rho_m$ and a-type edge dislocations with the density $\rho_e+\rho_m$. After the density of a+c-dislocations $\rho_m$ is determined from the fits of the symmetric reflections, asymmetric reflections are used to obtain the density of edge dislocations $\rho_e$.

The fit results are collected in Table I. Each reflection is fitted separately. The error bars are the mean squared deviations of the fits of individual reflections. Instead of presenting the screening distances $R$ for the dislocation strain fields, Table I shows, as suggested by Wilkens,[23–25] the ratios of the screening distances to the respective mean distances between dislocations $\rho^{-1/2}$, given by the dimensionless parameters $M = R\rho^{1/2}$. Dislocation densities obtained from the x-ray diffraction curves generally agree with the TEM data. However, the values notably disagree in some cases. Particularly, the density of a-type dislocations determined from the x-ray data for sample 2 is 4 times smaller than the TEM values, while the density of a+c-type dislocations for sample 4 is 5 times larger.

Let us discuss possible internal sources of error in the x-ray analysis. The description of the intensity profile by Eq. (1) is an approximation, the accuracy of which has been checked by Monte Carlo calculations.[16] The model of dislocation strain fields screened by surrounding dislocations has been implemented in both Monte Carlo calculation and Eq. (1). Since the dislocation density is an input parameter in the Monte Carlo calculation, the fit of the calculated diffraction profile to the approximate formula allows us to check the accuracy of the formula. A good agreement is found between the dislocation density assumed for the Monte Carlo calculation and that obtained by the fit. Hence, the approximations leading to Eq. (1) do not lead to noticeable errors.

The elastic relaxation of the dislocation strain fields at the free surface is not included in the analysis above.

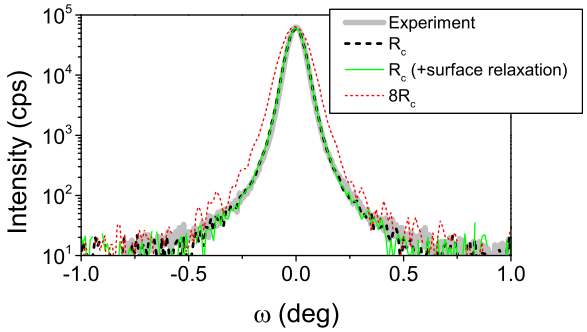


FIG. 3. Double-crystal rocking curves in skew geometry for the $11\bar{2}4$ reflection of sample 1: experimental curve (thick gray line) is compared to Monte Carlo calculations with (blue line) and without (black line) taking into account elastic surface relaxation of the dislocation strain fields. A Monte Carlo calculation for the same dislocation density but an 8 times larger screening distance $R_c$ is shown by the red line.

To check its contribution, we have performed Monte Carlo calculations of the double-crystal peak profiles in skew geometry with and without surface relaxation terms in the dislocation displacement fields. Figure 3 compares the experimental diffraction curve from sample 1 for the $11\bar{2}4$ reflection with the curves calculated by the Monte Carlo method. The details of the Monte Carlo calculation are described below in Sec. IV. The inclusion of the surface relaxation terms does not significantly change the calculated diffraction curve. Figure 3 also shows a diffraction curve calculated with the same dislocation densities but an 8 times larger parameter $R_c$ for the screening of dislocation strain fields. A notable broadening of the diffraction curve is evident.

Equation (1) is an approximate description of the diffraction curves, with only two parameters characterizing an array of dislocations, the dislocation density and their screening. A fit in linear or logarithmic scale provides better agreement of the curves either in the center or at the wings and result in different values for the dislocation density. The dislocation densities thus obtained can differ by a factor of 2. The disagreement is partially due to the limited range of intensities in the experiment, the background intensity, and the experimental noise. An accuracy within a factor of 2 is probably a practical limit of accuracy for the determination of the dislocation density from the diffraction curves.

In some cases, Table I shows a larger difference between TEM and the x-ray diffraction results. This discrepancy can possibly be due to the fact that TEM provides local information on the dislocation density, while x-ray diffraction collects intensity from a large area of the sample. Thus, differences between TEM and x-ray diffraction results may be caused by an inhomogeneity of the dislocation density over the sample.

### B. Triple–crystal diffraction

The skew diffraction measurements can also be performed in a triple–crystal setup with an analyzer crystal. Then, instead of the two-dimensional integration of the scattered intensity over the Ewald sphere in the double-crystal setup, a one-dimensional integration over the vertical divergence is performed. As a result, the peak profiles have different asymptotes at large wave vectors $q$: the intensity is proportional to $q^{-4}$ for a triple–crystal setup and, due to an additional integration, to $q^{-3}$ for a double–crystal setup. These dependences are a general property of scattering from dislocations.[17,18,26] An observation of these asymptotes serves as additional confirmation that the scattered intensity is due to dislocation strain fields. Figure 4 compares double– and triple–crystal peak profiles in skew geometry for sample 2. The expected asymptotes are clearly revealed.

A quantitative description of the triple-crystal diffraction profile is more complicated than for the double–crystal one. One starts, instead of using Eq. (1), with a two-dimensional integral over $x$ and $y$, containing an exponent $\exp(i\mathbf{q}\cdot\rho)$ with the two-dimensional vector $\rho = (x, y)$. The orientational factor $\gamma$ depends now on the direction of $\rho$. Particularly, the angle $\alpha$ in Eq. (7) is the angle between the diffraction vector $\mathbf{Q}$ and $\rho$. As a result, a complicated two-dimensional integral arises. It can be simplified by performing an orientational average of $\gamma$ first, i.e., replacing $\cos^2\alpha$ in Eq. (7) with its mean value 1/2. Then, the correlation function (2) can be used with the argument $|\rho|$ and the angular integration in polar coordinates gives[18,26]

$$I(\omega) = I_0 \int_0^\infty G_{\mathrm{th}}(x)\, x J_0(\omega x)\, dx + I_{\mathrm{backgr}}, \qquad (9)$$

where $J_0(x)$ is the zero order Bessel function. Equation (2) for the correlation function is used with $\cos^2\alpha$ replaced by 1/2 in the expression (7) for $\gamma_e$.

The fits of the double– and triple–crystal diffraction curves in Fig. 4 are performed by using Eqs. (1) and (9), respectively. A comparison of the dislocation densities obtained from these curves, as well as similar comparisons of the fits for different samples and different reflections, shows that the dislocation densities obtained from these two curves

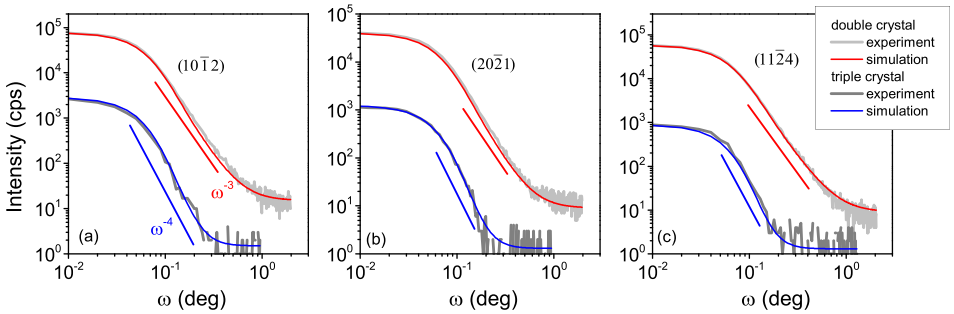


FIG. 4. Double- and triple-crystal rocking curves measured for sample 2 across different reflections and the fits by Eqs. (1) and (9), respectively.

may differ by a factor 2–3. Since the calculation of the triple-crystal curves involves an additional approximation of the orientational factor $\gamma$ described above, we consider it less reliable and restrict Table I to the double-crystal results.

From the experimental point of view, the introduction of the analyzer crystal in the diffraction setup results in a 1–2 orders of magnitude lower signal. The intensities are plotted in Fig. 4 in counts per second, so that they can be directly compared. The triple–crystal setup may be helpful to resolve different layers in a multilayer with close lattice parameters. Then, Eq. (9) can be used to estimate dislocation densities. Otherwise, the double–crystal setup is more advantageous both from experimental and theoretical points of view.

## IV. RECIPROCAL SPACE MAPS

The aim of this section is to analyze the experimental reciprocal space maps of samples 1–4 presented in the middle column of Fig. 1. The samples are arranged in the figure in sequence of increasing diffraction peak broadening and rotation of the isointensity ellipse. A comparison with Table I shows that this sequence does not coincide with the increasing dislocation densities: particularly, sample 3 possesses the lowest dislocation density, while samples 1 and 4 have fairly close dislocation densities but different reciprocal space maps. A comparison of the TEM images shows that threading dislocations in different samples are aligned along the surface normal to the same degree, so that the peak broadening is not related to a tilt of dislocations.

The shape of reciprocal space maps originating from an array of straight parallel dislocations follows already from the fact that their elastic fields do not depend on the coordinate $z$ along dislocation lines. Then, the intensity distribution in reciprocal space is a disk perpendicular to the dislocation lines. For dislocations in an infinite medium, the intensity distribution contains a delta function $\delta(q_z)$. In a film of a finite thickness, there will be a finite-size peak broadening. However, the films under consideration have thicknesses of several microns, so that this broadening is negligible. An additional broadening in $q_z$ direction can be caused by the elastic relaxation of the dislocation strain field at the free surface, since the relaxation field is $z$-dependent.[27] To evaluate this effect for the samples under consideration, we perform a Monte Carlo calculation of the reciprocal space maps.

The x-ray intensity of the coplanar triple-crystal diffraction is calculated in kinematical approximation as a Fourier transformation

$$I(q_x, q_z) = \int_{-\infty}^{\infty} dx \int_0^d dz_1 dz_2 G(x, z_1, z_2) \times \exp[iq_x x + iq_z(z_1 - z_2)], \quad (10)$$

of the correlation function

$$G(x, z_1, z_2) = \langle \exp\{i\mathbf{Q} \cdot [\mathbf{U}(\mathbf{r}_1) - \mathbf{U}(\mathbf{r}_2)]\} \rangle. \quad (11)$$

The coordinates $x$ and $z$ are in the scattering plane, along and normal to the surface, respectively. The points $\mathbf{r}_1(x_1, y, z_1)$ and $\mathbf{r}_2(x_2, y, z_2)$ possess the same coordinate $y$, as a result of the intensity integration over $q_y$ (over the vertical beam divergence in the experiment).[28] Since the system is laterally homogeneous, the correlation function $G(x, z_1, z_2)$ depends on the difference $x = x_1 - x_2$. There is no such homogeneity along the surface normal. The displacement $\mathbf{U}(\mathbf{r})$ is the total displacement at $\mathbf{r}$ due to all dislocations, and the statistical average $\langle \ldots \rangle$ is over their positions.

We perform the statistical average (11) and the spatial integration (10) simultaneously in a Monte Carlo calculation. The screening of the dislocation strain fields is modeled by generating dislocations in pairs, with random orientation of the pair and random distance between dislocations in the pair.[16] The mean distance between dislocations in the pair corresponds to an effective screening distance $R_c$. It is larger than the mean distance between dislocations by a factor of $M$, so that the pairs overlap. The points $\mathbf{r}_1$ and $\mathbf{r}_2$ are generated on random, with the mean distance between them restricted by the coherence length. We take Gaussian distributions both for the distances between dislocations in a pair and for the distances between the points $\mathbf{r}_1$ and $\mathbf{r}_2$. The standard deviation is the screening distance $R_c$ in the former case and the coherence length in the latter case.

Figure 5(a) presents the reciprocal space map calculated for sample 1 using dislocation displacement fields in an infinite medium. Dislocation densities and their correlations are taken from the x-ray data of Table I for this sample. The intensity distribution is a stripe extended in the $q_x$ direction, as discussed above and does not explain the observed reciprocal space maps in Fig. 1. In Fig. 5(b), the surface relaxation fields of dislocations normal to the surface of a half-space[29] are added. They cause the appearance of additional low intensity wings in $q_z$ direction on the reciprocal space map, but the effect is too small compared to the experiment. In Fig. 5(c), the calculation is performed with the same densities of

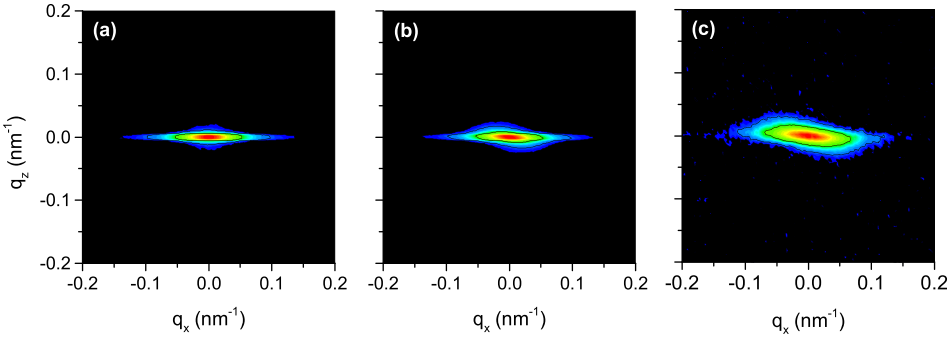


FIG. 5. Reciprocal space maps of the $11\bar{2}4$ reflection calculated by means of the Monte Carlo method for densities and screening distances for edge and mixed threading dislocations corresponding to sample 1 (see Table I). Maps are calculated (a) without and (b) with the surface relaxation term in dislocation displacements. (c) Reciprocal space map calculated with 8 times increased screening distances.

a- and a+c-dislocations, but with the screening distances $R_c$ increased by a factor of 8. The broadening of the diffraction pattern increases and the rotation of the reciprocal space map becomes visible. This result agrees with the calculations by Barchuk *et al.*[27] performed for uncorrelated dislocations. However, the loss of dislocation screening also leads to a broadening of the double-crystal rocking curves. Figure 3 compares the peak profiles calculated with parameters corresponding to Figs. 5(b) and 5(c). The increasing $R_c$ evidently leads to a disagreement in the peak widths. Besides that, the reciprocal space map in Fig. 5(c) may be used to explain the experimental reciprocal space map of sample 1 but certainly cannot explain the maps of the other samples with comparable or even smaller dislocation densities but larger broadening and rotation of the reciprocal space maps.

Additional broadening of the reciprocal space maps can be caused by misfit dislocations releasing mismatch between the GaN film and the substrate. The real interfacial structure is fairly complicated, especially taking into account the initial layers grown to reduce the threading dislocation density, and we do not discuss it here. We do not take into account explicitly the presence of several interfaces between substrate, AlN buffer layers and the GaN epilayers. For the sake of simplicity, the whole epitaxial structure is replaced in our model by an array of straight misfit dislocations needed to relax the misfit to the substrate. The strain inhomogeneity in the layer and the peak broadening due to misfit dislocations depend on their correlations:[28,30] it is maximum for uncorrelated randomly positioned dislocations and tends to zero as dislocation arrangement becomes close to a periodic one. Hence, we consider an effective dislocation density, which takes into account correlations in dislocation positions.

In calculation of the correlation function (11), the total displacements $\mathbf{U}$ can be considered as a sum of statistically independent displacements due to misfit and threading dislocations, so that the correlation function is a product of the corresponding correlation functions, $G = G_{\mathrm{misf}} G_{\mathrm{th}}$. An appropriate approximation for the correlation function of threading dislocations is given by Eq. (2).

For misfit dislocations, the approximation developed in Ref. 28 for large dislocation densities can be employed. The correlation function is represented in an exponential form, $G_{\mathrm{misf}} = \exp(-T_{\mathrm{misf}})$, where the real part of the exponent is calculated as

$$\mathrm{Re}\, T_{\mathrm{misf}} = \frac{\rho_{\mathrm{misf}}}{2}\left(w_{xx}x^2 + w_{xz}x\zeta + w_{zz}\zeta^2\right), \tag{12}$$

where $\zeta = z_1 - z_2$ and $\rho_{\mathrm{misf}}$ is the linear density of misfit dislocations. The coefficients $w_{ij}(z)$ depend on the mean position $z = (z_1 + z_2)/2$. Taking into account three dislocation arrays at the hexagonal interface, 120° to each other, these coefficients can be written as

$$\begin{aligned} w_{xx}(z) &= \frac{1}{8}\left[(3Q_x^2 + Q_y^2)W_{xxxx}(z) + 4Q_z^2 W_{zxzx}(z)\right], \\ w_{xz}(z) &= \frac{1}{2}Q_x Q_z [W_{xxzz}(z) + W_{xzxz}(z)], \\ w_{zz}(z) &= \frac{1}{2}\left[(Q_x^2 + Q_y^2)W_{xzxz}(z) + 2Q_z^2 W_{zzzz}(z)\right], \end{aligned} \tag{13}$$

where it is denoted

$$W_{ijkl} = \int_{-\infty}^{\infty} dx \frac{\partial u_i}{\partial x_k}\frac{\partial u_j}{\partial x_l}. \tag{14}$$

Here $x_i = \{x, z\}$ and $u_i$ is the $i$-th component of the displacement due to a misfit dislocation with the dislocation line in $y$ direction. The integrals (14) can be calculated analytically. The imaginary part of $T_{\mathrm{misf}}$ is linear over $x$ and $\zeta$ and determines the diffraction peak position. It is not considered here explicitly. Particularly, thermal strain due to the difference in the thermal expansion coefficients between the layers and the substrate does not affect the calculation of the peak broadening since it causes a homogeneous strain contributing to the imaginary part of the correlation function and causing a shift of the diffraction peak.

The integration over $\zeta$ in Eq. (10) can be performed analytically. Then, the intensity distribution due to misfit and threading dislocations is given by a two-dimensional integral

$$\begin{aligned} I(q_x, q_z) = \int_0^d dz \int_{-\infty}^{\infty} dx\, G_{\mathrm{th}}(x)\tilde{G}_{\mathrm{misf}}(z) \\ \times \exp\left[\left(iq_x - q_z\frac{w_{xz}(z)}{2w_{zz}(z)}\right)x\right], \end{aligned} \tag{15}$$

where $G_{\mathrm{th}}(x)$ is given by Eq. (2). The function $\tilde{G}_{\mathrm{misf}}$ appears after the integration over $\zeta$ is performed and is given by

$$\tilde{G}_{\mathrm{misf}}(z) = \sqrt{\frac{\pi}{w_{zz}(z)}}\exp\left(-\frac{q_z^2}{4w_{zz}(z)}\right). \tag{16}$$

The right column of Fig. 1 presents reciprocal space maps calculated by Eq. (15) using standard quadratures, and the right column of Table I contains the effective densities of misfit dislocations in samples 1–4 used for these calculations. These values are discussed below in Sec. V.

After the effect of misfit dislocations on the reciprocal space maps is established, we have to return to the diffraction curves in skew geometry and evaluate the effect of misfit dislocations for these curves. Figure 6 compares the experimental diffraction curves of samples 1 and 4 with the ones calculated when misfit dislocations are taken into account. The densities of threading dislocations have been calculated first as it is described in Sec. III A. Then, the diffraction curves are calculated by taking into account both threading and misfit dislocations, as well as surface strain relaxation for both dislocation types. Threading dislocations and the spatial integration are treated by the Monte Carlo method, while for misfit dislocations the correlation function (12) is used. Thus, a distribution of threading dislocations is generated according to the densities and screening distances obtained from the initial fits. A pair of spatial points is generated. The random distance between these points is chosen according to the spatial resolution, and the vector connecting these points is in the direction of the diffracted beam, exactly as it has been done above for the calculations presented in Fig. 3. Then, the correlation function for misfit dislocations is calculated by Eq. (12) for these points, and used as an additional multiplier in the Monte Carlo calculation.

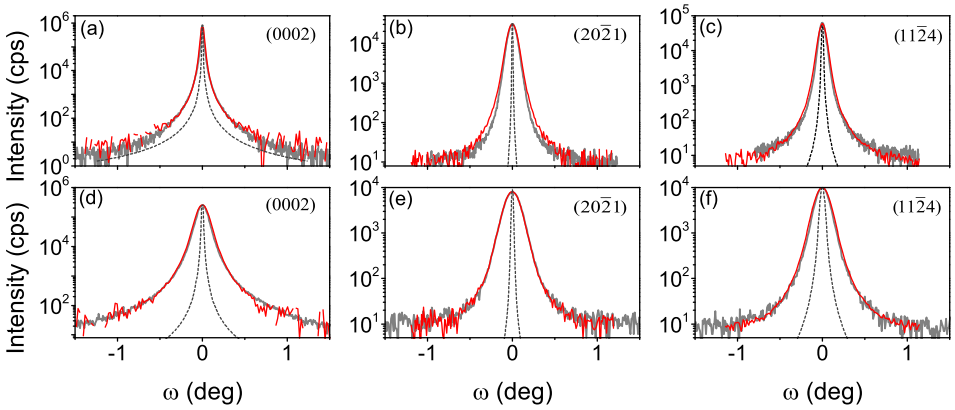


FIG. 6. X-ray diffraction profiles across the (a), (d) symmetric 0002 and asymmetric (b), (e) 20$\bar{2}$1, (c), (f) 11$\bar{2}$4 reflections taken from samples 1 (a)–(c) and 4 (d)–(f). Experimental profiles (thick gray lines) are compared with Monte Carlo calculations that include both misfit and threading dislocations. The densities and correlation parameters are those in Table I. The dashed lines show the calculated diffraction profiles due to only misfit dislocations.

The agreement of the calculated and the experimental curves in Fig. 6 shows that the contribution of misfit dislocations to the double–crystal diffraction curves in skew geometry is very small. The dashed lines also show the calculated peaks for only misfit dislocations, without contribution of threading dislocations. They are notably narrower than the experimental curves. Hence, the dislocation density determination from double–crystal curves in skew geometry described in Sec. III A remains applicable also in the presence of misfit dislocations.

## V. DISCUSSION AND CONCLUSIONS

The results of the present paper show that the densities of threading dislocations in MOVPE grown GaN films can be determined from double–crystal x-ray diffraction profiles measured in skew geometry. Comparable densities of screw and edge dislocations require a modification of the previous method[17] by including screw dislocations in the calculations of asymmetric reflections. The x-ray diffraction does not distinguish between mixed a+c-dislocations and separate edge a-type dislocations and screw c-type dislocations with equal densities. Hence, edge and screw dislocations are included in the calculations.

The internal consistency of the calculations is proven by performing a direct Monte Carlo calculation of the peak profiles without approximations or simplifications. A good agreement between the experimental diffraction curves, the ones calculated by the Monte Carlo method, and the description by an approximate correlation function is demonstrated. An array of threading dislocations is characterized by two parameters, a dislocation density and a screening length of the dislocation displacement fields by other dislocations.

The agreement between the experimental and the calculated peak profiles is very good. However, fits on a linear and logarithmic scale give somewhat different dislocation densities. Moreover, fits of the different reflections also show a scattering in the values of the dislocation density. Comparing different samples and different reflections, as well as Monte Carlo and approximate calculations, we estimate the accuracy of the x-ray determination of dislocation density to be within a factor of 2. In some samples, a larger discrepancy between the x-ray and TEM results is found. In our opinion, this deviation is caused by an inhomogeneity of the dislocation density over the sample. The TEM analysis is of a very local nature, while x-ray diffraction averages over a large sample area.

The elastic strain relaxation at the free surface is taken into account in the Monte Carlo calculations. The surface relaxation causes rather little, albeit observable, modification of the reciprocal space maps. Its effect on the double-crystal profiles in skew geometry is negligible.

Threading dislocations alone are not enough to explain the broadening of the reciprocal space maps and their orientation. We argue that the defects at the film–substrate interface accommodating the lattice mismatch of the materials also cause the broadening of the reciprocal maps. We model the interface by a network of straight misfit dislocations. The reciprocal space maps due to both misfit and threading dislocations are calculated. Since strain inhomogeneity due to misfit dislocations reduces with their ordering, we find an effective density of misfit dislocations by comparing the experimental and the calculated reciprocal space maps. The effective density differs by almost a factor of 8 between the samples studied in this work.

The mismatch of 13.8% between GaN and sapphire[31] gives rise to a linear density of misfit dislocations $8.8 \times 10^6$ $cm^{-1}$. The largest effective misfit dislocation density in Table I is almost 40 times smaller than this value. Hence, the misfit dislocations are well ordered and notably reduce the strain inhomogeneity with respect to that due to randomly positioned dislocations at the interface. The correlation parameter $g$ (Refs. 28 and 30) varies for samples 1–4 from 0.004 to 0.25.

The broadening of the reciprocal space maps and the effective densities of misfit dislocations can be related to the growth modes. Samples 1 and 2 reveal notably smaller misfit dislocation densities, in comparison to samples 3 and 4 (see Table I). The growth of samples 1 and 3 possesses an extended initial stage of 3D growth prior to the 2D growth, while samples 2 and 4 do not have such stage. Hence, the 3D–2D transition is not relevant here. Samples 1 and 2 have a sharp AlN/GaN interface, while the samples 3 and 4 do not have it. AlN was not used in the growth of sample 3, and in sample 4 a transition layer of $Al_xGa_{1-x}N$ was used. We conclude that the AlN/GaN interface reduces strain inhomogeneity due to misfit dislocations and gives rise to more homogeneous strains in GaN film.

After we have established the effect of misfit dislocations on the reciprocal space maps, we turned back to the diffraction curves in skew geometry. A Monte Carlo calculation of these curves with both misfit and threading dislocations shows that the effect of misfit dislocations is negligible. Thus, the dislocation density can be determined from the diffraction peak profiles in skew geometry without the need to consider misfit dislocations.

## ACKNOWLEDGMENTS

We gratefully acknowledge a critical reading of the manuscript by Oliver Brandt. Monte Carlo simulations have been performed using the local computational cluster facility administrated by Frank Grosse. X-ray measurements have been carried out in the Joint Research Center "Materials science and characterization in advanced technology" (Ioffe Institute, St.-Petersburg, Russia). The work has been partially funded by Deutsche Forschungsgemeinschaft (DFG) Grant No. KA 3262/2-2.

[1]S. C. Jain, M. Willander, and J. Narayan, J. Appl. Phys. **87**, 965 (2000).
[2]W. V. Lundin, A. E. Nikolaev, A. V. Sakharov, S. O. Usov, E. E. Zavarin, P. N. Brunkov, M. A. Yagovkina, N. A. Cherkashin, and A. F. Tsatsulnikov, Semiconductors **48**, 53 (2014).
[3]N. M. Shmidt, V. V. Sirotkin, A. A. Sitnikova, O. A. Soltanovich, R. V. Zolotareva, and E. B. Yakimov, Phys. Status Solidi C **2**, 1797 (2005).
[4]M. A. Moram and M. E. Vickers, Rep. Prog. Phys. **72**, 036502 (2009).
[5]V. Srikant, J. S. Speck, and D. R. Clarke, J. Appl. Phys. **82**, 4286 (1997).
[6]V. Holý, J. Kuběna, E. Abramof, K. Lischka, A. Pesek, and E. Koppensteiner, J. Appl. Phys. **74**, 1736 (1993).
[7]S. Rubini, B. Bonanni, E. Pelucchi, A. Franciosi, A. Garulli, A. Parisini, Y. Zhuang, G. Bauer, and V. Holý, J. Vac. Sci. Technol. B **18**, 2263 (2000).
[8]R. Chierchia, T. Böttcher, T. S. Figge, M. Diesselberg, H. Heinke, and D. Hommel, Phys. Status Solidi B **228**, 403 (2001).
[9]R. Chierchia, T. Böttcher, H. Heinke, S. Einfeldt, S. Figge, and D. Hommel, J. Appl. Phys. **93**, 8918 (2003).
[10]T. Metzger, R. Höpler, E. Born, O. Ambacher, M. Stutzmann, R. Stömmer, M. Schuster, H. Göbel, S. Christiansen, M. Albrecht, and H. P. Strunk, Philos. Mag. A **77**, 1013 (1998).
[11]X. H. Zheng, H. Chen, Z. B. Yan, Y. J. Han, H. B. Yu, D. S. Li, Q. Huang, and J. M. Zhou, J. Cryst. Growth **255**, 63 (2003).
[12]S. R. Lee, A. M. West, A. A. Allerman, K. E. Waldrip, D. M. Follstaedt, P. P. Provencio, D. D. Koleske, and C. R. Abernathy, Appl. Phys. Lett. **86**, 241904 (2005).
[13]P. Gay, P. B. Hirsch, and A. Kelly, Acta Metall. **1**, 315 (1953).
[14]A. D. Kurtz, S. A. Kulin, and B. L. Averbach, Phys. Rev. **101**, 1285 (1956).
[15]C. G. Dunn and E. F. Koch, Acta Metall. **5**, 548 (1957).
[16]V. M. Kaganer and K. K. Sabelfeld, Acta Cryst. A **66**, 703 (2010).
[17]V. M. Kaganer, O. Brandt, A. Trampert, and K. H. Ploog, Phys. Rev. B **72**, 045423 (2005).
[18]I. Booker, L. R. Khoshroo, J. F. Woitok, V. Kaganer, C. Mauder, H. Behmenburg, J. Gruis, M. Heuken, H. Kalisch, and R. H. Jansen, Phys. Status Solidi C **7**, 1787 (2010).
[19]W. V. Lundin, A. E. Nikolaev, M. A. Yagovkina, P. N. Brunkov, M. M. Rozhavskaya, B. Y. Ber, D. Y. Kazantsev, A. F. Tsatsulnikov, A. V. Lobanova, and R. A. Talalaev, J. Cryst. Growth **352**, 209 (2012).
[20]Y. J. Sun, O. Brandt, T. Y. Liu, A. Trampert, and K. H. Ploog, Appl. Phys. Lett. **81**, 4928 (2002).
[21]J. Martinez-Garcia, M. Leoni, and P. Scardi, Acta Crystallogr. A **65**, 109 (2009).
[22]M. A. Krivoglaz and K. P. Ryboshapka, Fiz. Met. Metalloved. **15**, 18 (1963), [Phys. Met. Metallogr. **15**, 14 (1963)].
[23]M. Wilkens, in *Fundamental Aspects of Dislocation Theory*, edited by J. A. Simmons, R. de Wit, and R. Bullough (Nat. Bur. Stand. (U.S.) Spec. Publ., Washington, D.C., 1970), p. 1195.
[24]M. Wilkens, Phys. Status Solidi A **2**, 359 (1970).
[25]M. Wilkens, Kristall Tech. **11**, 1159 (1976).
[26]V. M. Kaganer, A. Shalimov, J. Bak-Misiuk, and K. H. Ploog, J. Phys.: Condens. Matter **18**, 5047 (2006).
[27]M. Barchuk, V. Holy, B. Miljevic, B. Krause, T. Baumbach, J. Hertkorn, and F. Scholz, J. Appl. Phys. **108**, 043521 (2010).
[28]V. M. Kaganer, R. Köhler, M. Schmidbauer, R. Opitz, and B. Jenichen, Phys. Rev. B **55**, 1793 (1997).
[29]J. Lothe, *in Elastic Strain Fields and Dislocation Mobility*, edited by V. L. Indenbom and J. Lothe (North-Holland, Amsterdam, 1992), Chap. 5.
[30]V. M. Kaganer and K. K. Sabelfeld, Phys. Status Solidi A **208**, 2563 (2011).
[31]C. J. Rawn and J. Chaudhuri, Adv. X-ray Anal. **43**, 338 (2000).